AIAA JOURNAL
Vol. 33, No. 5, May 1995

Numerical Simulation of Trailing-Edge Acoustic/Vortical Interaction

Pong-Jeu Lu,* Dartzi Pan,† and Dun-Yann Yeh‡
National Cheng Kung University, Tainan, Taiwan 70101, Republic of China

The objective of the present research is twofold. The first part concerns the construction of a high-resolution aeroacoustic flow solver, and the remaining emphasizes the wave/vortex interaction around a sharp trailing edge. Euler equations and the Osher-Chakravarthy MUSCL-type high-resolution upwind TVD scheme were used, respectively, as the flow model and the numerical algorithm to analyze the acoustically excited flow. Modification on the reconstruction of the cell interface values was first made to improve the scheme fidelity so that a wave propagation problem can be solved on nonuniform mesh systems. An acoustic source modeling was also devised to simulate the generation of sound emitted from a monopole located on the solid boundary. The numerical algorithm was first evaluated by checking the computed results with several test problems that have analytic solutions. Results show that the currently proposed computational aeroacoustic scheme is accurate and reliable. An acoustically excited incompressible and low-Mach-number flow over a finite plate was then simulated. The results show that the unsteady airloads induced by acoustic/vortical interaction around a sharp trailing edge can be satisfactorily resolved by the currently developed inviscid Euler flow solver.

I. Introduction

ACOUSTIC flutter suppression is a novel idea that has been successfully demonstrated in a wind-tunnel experiment.[1] Compared with the hydraulically actuated mechanical type aerodynamic control surfaces, acoustic devices have the advantages of being simple in hardware and easy to be implemented, and, most importantly, the operational frequency range is broad and the response is quick. To explain the underlying mechanism, Lu and Huang[4] performed a theoretical analysis concerning the unsteady aerodynamic field induced by acoustic excitations in linearized incompressible flow. It shows that the sharp trailing edge is the place where the conversion of an incident acoustic wave into shedding vorticity waves takes place. According to Kelvin's theorem, a bound vortex is produced that counterbalances the shedding vortices and manifests aerodynamically as the acoustically induced lift and pitching moment acting on the solid body. Flutter instabilities were shown to be suppressed when these acoustically induced unsteady airloads were produced with appropriate phase lags relative to the vibrational motion. Based on these findings and the results obtained, the acoustic excitation technique was demonstrated to be a new and promising flutter suppression method.

The main objective of the present study is to explore the possibility of whether this acoustic/vortical interaction can be resolved numerically. The ultimate goal is to use this scheme to look into more intricate problems, such as transonic flutter, in which nonlinearity is crucial. Using numerical means to resolve the flow details regarding the acoustic/vortical interaction demands high resolution and low dissipation and dispersion of the scheme. In addition, the nonreflective boundary condition treatment and the acoustic source modeling are also important. Unlike the conventional acoustic computations, the present approach does not follow the classical line of extracting and hence computing the perturbation field only, while assuming that the mean flow is given a priori. Generally speaking, the nonlinear interactions among acoustic, vortical, and shock waves can only be analyzed as the unsteady aerodynamic field is treated as a whole.

Many state-of-the-art finite difference or finite volume methods were devised originally for coping with the steady-state problems. Hence, a certain amount of dissipation and dispersion exists in those schemes, which poses fundamental difficulties for them to be used for the aeroacoustic computations. Dissipation is often a necessity required by a stable scheme, in particular the steady-state algorithm, and dispersion arises as a result of the choice of stencil points and the Courant-Friedrichs-Lewy (CFL) number selected. Recently, nondissipative[2] and dispersion-relation-preserving[3] schemes were proposed for solving the linearized Euler equations. Waves of long-distance propagation can thus be more accurately simulated for a wider frequency range. However, those improvements due to elimination of the numerical dissipation, in principle, cannot be enjoyed when shock waves or contact discontinuities are present, since, numerically, dissipation is required by the entropy condition and the monotonicity of the shock-capturing schemes. As far as the present problem is concerned, the key physical mechanism occurs mainly in the near field around the solid airfoil body, and the frequency of the applied acoustic excitation is low. Hence, a sacrifice in the accuracy of the far acoustic field can be tolerated as long as the radiated sound is not to be significantly reflected back to contaminate the near field. These particular physical considerations allow the present use of high-resolution MUSCL-type upwind schemes in the acoustic flowfield computations subject only to minor adaptations. Improvements are made on the interpolations of the reconstructed variables on the two sides of the cell interface, as will be shown later. These modifications make the upwind flow solver more transparent for waves to be computed on a nonuniform mesh system, due to the reduction of the reflective noises among unevenly spaced meshes.

There were three test problems considered for examining the accuracy of the present scheme. They include the problems of linear wave convection, baffled piston radiation, and a uniform stream past a plane of infinite extent on which a monopole sound source was flush mounted. All of these test problems have analytic solutions so that the numerical algorithms can be evaluated properly.

Trailing-edge receptivity, or wave/vortex interaction around a sharp trailing edge, was then studied using this newly developed scheme. The computed results were found in good agreement with the analytic solutions.[4]

II. Governing Equations and the Numerical Formulations

The present problem is concerned with the acoustic/vortical wave interaction around a solid surface.[5–8] This acoustically induced vorticity production at the trailing edge might be taken as an inviscid phenomenon, since the role of viscosity can be accounted for in the enforcement of the Kutta condition.[9,10] Based on the previous

Received June 14, 1993; revision received July 11, 1994; accepted for publication July 18, 1994.

*Professor, Institute of Aeronautics and Astronautics. Member AIAA.
†Associate Professor, Institute of Aeronautics and Astronautics. Member AIAA.
‡Graduate Research Assistant, Institute of Aeronautics and Astronautics.

arguments, Euler equations are adopted as the governing equations to be solved. In the construction of the numerical flow solver, emphasis will be placed upon the reduction of the numerical dissipation and dispersion effects, as well as the treatment of the boundary conditions.

Finite Volume Method

The unsteady, two-dimensional inviscid Euler flow in a domain V bounded by a boundary S can be expressed in an integral conservation form,

$$\frac{\partial}{\partial t}\int_V U\,\mathrm{d}V + \oint_S \boldsymbol{n}\cdot\boldsymbol{F}\,\mathrm{d}S = 0 \tag{1}$$

In the previous equation the set of conservative variables U and the normal flux vector $F_n = \boldsymbol{n}\cdot\boldsymbol{F}$ are given, respectively, by the column vectors

$$U = \begin{bmatrix} \rho \\ \rho u \\ \rho v \\ \rho e \end{bmatrix}, \qquad F_n = \begin{bmatrix} \rho u_n \\ \rho u u_n + p n_x \\ \rho v u_n + p n_y \\ \rho e u_n + p u_n \end{bmatrix} \tag{2}$$

where $u_n = \boldsymbol{u}\cdot\boldsymbol{n}$ is the normal velocity component with n_x and n_y defined as the projections of the unit normal $\boldsymbol{n}$ in the x and y directions. The variables p, ρ, u, v, and e denote the static pressure, density, Cartesian velocity components, and specific total energy, respectively. In closing the previous governing equations, the thermodynamic state equation of a perfect gas is required,

$$p = (\gamma - 1)\left(\rho e - \frac{\rho}{2}\boldsymbol{u}\cdot\boldsymbol{u}\right) \tag{3}$$

in which the specific heat ratio is given by $\gamma = 1.4$.

In the finite volume approach, the integral conservation form, Eq. (1), is first applied to a discretized control volume $V_{i,j}$,

$$\frac{\partial}{\partial t}\int_{V_{i,j}} U\,\mathrm{d}V + \oint_{S_{i,j}} \boldsymbol{n}\cdot\boldsymbol{F}\,\mathrm{d}S = 0 \tag{4}$$

and then Eq. (4) is approximated using a spatially differenced scheme to yield a semidiscretized system of ordinary differential equations,

$$\frac{\partial}{\partial t}(U_{i,j}V_{i,j}) + \sum_k \tilde{F}_k S_k = 0 \tag{5}$$

where the index k associated with the flux terms refers to the external side of the control volume $V_{i,j}$, and $U_{i,j}$ is taken as the cell-averaged variable of the control volume. The design principle for the construction of the numerical flux function $\tilde{F}_k$ decides the nature and order of accuracy of the scheme. The method currently adopted is explained in the following.

Osher-Chakravarthy Upwind TVD Scheme

The spatial accuracy of the finite volume discretization depends on the construction of the numerical flux function $\tilde{F}_k$ of the discretized equation, Eq. (5). In this study, the numerical fluxes were computed using Roe's scheme[11] and the characteristic variable interpolation of Chakravarthy and Osher.[12] It is believed that, compared with other schemes, the characteristics-based flux-difference scheme possesses a comparatively complete portrait of the wave propagation phenomena that include the capture of the shock waves and the interactions among acoustic, entropy, and vorticity waves that mutually interact and evolve in the flowfield.

The advantage of flux-difference schemes for treating wave phenomena, perhaps, can best be explained using the characteristic form of the Euler equations. Along the four characteristic curves (Two-dimensional problem), the variations of the characteristic variables,

$$\begin{aligned} \alpha_1 &= \delta\rho - \delta p/c^2 \\ \alpha_2 &= n_x\delta u - n_y\delta v \\ \alpha_3 &= \boldsymbol{n}\cdot\delta\boldsymbol{u} + \delta p/\rho c \\ \alpha_4 &= -\boldsymbol{n}\cdot\delta\boldsymbol{u} + \delta p/\rho c \end{aligned} \tag{6}$$

are exactly those associated with the entropy, vorticity, and acoustic waves. Note that, in the one-dimensional sense, the physics are well represented in the numerical algorithm since dividing the flux difference into components according to the Riemann solver is a basic procedure contained in the construction of a flux-difference scheme. Moreover, no special assumption of linearity has been invoked as Roe's splitting is used, hence making the present scheme more versatile in treating both linear and nonlinear wave interaction problems.

At each i-direction cell interface $i+\frac{1}{2}$, let $U^+_{i+1/2}$ and $U^-_{i+1/2}$ denote the values of the conservative variables specified at the right and left sides of the cell interface, respectively. Theoretically, one can construct a one-dimensional upwind-biased scheme to, in principle, any desired order of accuracy by properly defining the left and right states at the cell interface via interpolations using the neighboring cell-averaged values. However, these high-order interpolations may incur numerical instability and/or result in complicated boundary condition treatments and use unreasonably distributed stencil points when extended to multidimensional problems. Hence, the present scheme only considers accuracy (in the one-dimensional sense and on a uniform grid) to at most the third order.

First of all, let us define the characteristic wave differences:

$$\begin{aligned} \alpha^m_{i+\frac{1}{2}} &= \ell^m_i(U_{i+1} - U_i) \\ \alpha^m_{i-\frac{1}{2}} &= \ell^m_i(U_i - U_{i-1}) \end{aligned} \tag{7}$$

where

$$\ell^m_i = \ell^m\left[U_i, \left(N_{i+\frac{1}{2}} + N_{i-\frac{1}{2}}\right)/2\right] \tag{8}$$

is the mth left eigenvector associated with the mth eigenvalue of the flux Jacobian matrix $\partial F_n/\partial U$, and N denotes the set of unit surface normal projections n_x and n_y. Using the previous variables $\alpha^m_{i\pm1/2}$, the interpolated conservative variables at the left and right sides of the cell interface can be derived using the MUSCL-type[13] interpolation,

$$\begin{aligned} U^-_{i+\frac{1}{2}} &= U_i + \chi_i \sum_m \left[(\zeta_i + 2\phi\sigma_i)\alpha^m_{i+\frac{1}{2}} \right. \\ &\quad \left. + \frac{1}{\zeta_i}(1 - 2\phi\sigma_i)\alpha^m_{i-\frac{1}{2}}\right] r^m_i \\ U^+_{i-\frac{1}{2}} &= U_i - \chi_i \sum_m \left[(\zeta_i - 2\phi\sigma_i)\alpha^m_{i+\frac{1}{2}} \right. \\ &\quad \left. + \frac{1}{\zeta_i}(1 + 2\phi\sigma_i)\alpha^m_{i-\frac{1}{2}}\right] r^m_i \end{aligned} \tag{9}$$

where

$$\begin{aligned} r^m_i &= r^m\left[U_i, \left(N_{i+\frac{1}{2}} + N_{i-\frac{1}{2}}\right)/2\right] \\ \zeta_i &= (s_i + s_{i-1})/(s_i + s_{i+1}) \\ \chi_i &= s_i/(s_{i+1} + 2s_i + s_{i-1}) \\ \sigma_i &= s_i/(s_i + s_{i+1}) \end{aligned} \tag{10}$$

In Eq. (10), the vector r^m_i is the mth right eigenvector of the flux Jacobian and the geometry-related parameters ζ_i, χ_i, and σ_i are functions of the mean cell width s_i (defined as the distance between the centers of the two opposite cell surfaces) in the i direction. This extension that considers mesh spacings in the construction of the interface variables is not new. It has been proposed previously in the design of a high-resolution non-MUSCL-type scheme.[14] For a uniform mesh system ($\zeta_i = 1$, $\chi_i = \frac{1}{4}$, and $\sigma_i = \frac{1}{2}$), the previous formulas recover the usual MUSCL-type form[12,13]:

$$\begin{aligned} U^-_{i+\frac{1}{2}} &= U_i + \sum_m \left(\frac{1+\phi}{4}\alpha^m_{i+\frac{1}{2}} + \frac{1-\phi}{4}\alpha^m_{i-\frac{1}{2}}\right) r^m_i \\ U^+_{i-\frac{1}{2}} &= U_i - \sum_m \left(\frac{1-\phi}{4}\alpha^m_{i+\frac{1}{2}} + \frac{1+\phi}{4}\alpha^m_{i-\frac{1}{2}}\right) r^m_i \end{aligned} \tag{11}$$

The magnitude of the acoustic field is usually so small that it is very easy to be contaminated. It is to be shown that Eq. (9) is meaningful for a time-accurate acoustic computation, since the interpolation errors caused by ignoring the grid nonuniformity, which would otherwise be eliminated iteratively and is usually not eminent in the steady-state flow problems, may introduce high-frequency noises among grids during the simulation of the sound waves.

The parameter ϕ takes on different values depending on the stencil points and the order of accuracy selected. The use of $\phi = \frac{1}{3}$ will result in a third-order accuracy in the sense of a one-dimensional simulation on a uniform grid. As a nonuniform mesh system is used, the order of accuracy of this popular MUSCL-type scheme, Eq. (11), will degrade due to the poorer interpolations, as will be shown in the subsequent numerical examinations.

The monotonicity property of the total variation diminishing (TVD) scheme is guaranteed using the slope limiter given by

$$\begin{aligned} \tilde{\alpha}^m_{i+\frac{1}{2}} &= \text{minmod}\left(\alpha^m_{i+\frac{1}{2}},\ \beta\alpha^m_{i-\frac{1}{2}}\right) \\ \tilde{\tilde{\alpha}}^m_{i-\frac{1}{2}} &= \text{minmod}\left(\alpha^m_{i-\frac{1}{2}},\ \beta\alpha^m_{i+\frac{1}{2}}\right) \end{aligned} \tag{12}$$

In these equations, the compression parameter β and the minmod operator are defined, respectively, by (see Appendix A of Ref. 16)

$$\beta = \zeta_i[1 - \chi_i(\zeta_i + 2\phi\sigma_i)]/[\chi_i(1 - 2\phi\sigma_i)] \tag{13a}$$

$$\text{minmod}(x, y) = \text{sign}(x) \cdot \max\{0, \min[|x|, y \cdot \text{sign}(x)]\} \tag{13b}$$

Therefore, the limited and interpolated variables $U^-_{i+\frac{1}{2}}$ and $U^+_{i-\frac{1}{2}}$ become

$$\begin{aligned} U^-_{i+\frac{1}{2}} &= U_i + \chi_i \sum_m \left[(\zeta_i + 2\phi\sigma_i)\tilde{\alpha}^m_{i+\frac{1}{2}} \right. \\ &\quad \left. + \frac{1}{\zeta_i}(1 - 2\phi\sigma_i)\tilde{\tilde{\alpha}}^m_{i-\frac{1}{2}} \right] r^m_i \\ U^+_{i-\frac{1}{2}} &= U_i - \chi_i \sum_m \left[(\zeta_i - 2\phi\sigma_i)\tilde{\alpha}^m_{i+\frac{1}{2}} \right. \\ &\quad \left. + \frac{1}{\zeta_i}(1 + 2\phi\sigma_i)\tilde{\tilde{\alpha}}^m_{i-\frac{1}{2}} \right] r^m_i \end{aligned} \tag{14}$$

Using Roe's approximate Riemann solver,[11] the numerical flux $\tilde{F}_{i+\frac{1}{2}}$ across the cell interface in the i direction can be constructed readily,

$$\begin{aligned} \tilde{F}_{i+\frac{1}{2}} &= F_n\left(U^-_{i+\frac{1}{2}},\ N_{i+\frac{1}{2}}\right) + \sum_m \lambda^{m-}_{i+\frac{1}{2}} \alpha^m_{i+\frac{1}{2}} r^m_{i+\frac{1}{2}} \\ &= F_n\left(U^+_{i+\frac{1}{2}},\ N_{i+\frac{1}{2}}\right) - \sum_m \lambda^{m+}_{i+\frac{1}{2}} \alpha^m_{i+\frac{1}{2}} r^m_{i+\frac{1}{2}} \\ &= \tfrac{1}{2}\left[F_n\left(U^+_{i+\frac{1}{2}},\ N_{i+\frac{1}{2}}\right) + F_n\left(U^-_{i+\frac{1}{2}},\ N_{i+\frac{1}{2}}\right)\right] \\ &\quad -\tfrac{1}{2}\left[\sum_m \left(\lambda^{m+}_{i+\frac{1}{2}} - \lambda^{m-}_{i+\frac{1}{2}}\right)\alpha^m_{i+\frac{1}{2}} r^m_{i+\frac{1}{2}}\right] \end{aligned} \tag{15}$$

where $\lambda^{m\pm}$ represents the mth eigenvalue corresponding to either the downwind (+) or the upwind (−) propagating characteristic waves.

Time Integration

The semidiscretized system of governing equations, Eq. (5), can be symbolically expressed as

$$\frac{\mathrm{d}(W)}{\mathrm{d}t} + R(U) = 0 \tag{16}$$

where $W = UV$, and $R(U)$ represents the residual contributed from the numerical fluxes across the cell surfaces. This system of ordinary differential equations will be numerically integrated in time using the explicit Runge–Kutta time-stepping method. For a K-stage Runge–Kutta scheme, the advancement of each variable from time level (n) to $(n + 1)$ is enforced using the following recursive formulas:

$$\begin{aligned} W^{(0)} &= W^n \\ W^{(1)} &= W^{(0)} - \alpha_1 \Delta t R[U^{(0)}] \\ &\vdots \\ W^{(k)} &= W^{(0)} - \alpha_k \Delta t R[U^{(k-1)}] \\ W^{n+1} &= W^{(k)} \end{aligned} \tag{17}$$

The present study adopts a three-stage scheme with $\alpha_1 = 0.24$, $\alpha_2 = 0.50$, and $\alpha_3 = 1.0$. This time marching has previously been used in the oscillating airfoil calculations[15] and was justified to be of second-order accuracy in time while maintaining the TVD property.

Boundary Conditions and Monopole Sound Source Modeling

For the present problem of interest, the methods for emitting sound waves from a solid surface may be divided into two categories. One is of the structural vibration type, such as a flush-mounted loudspeaker, a vibrating ribbon or piston, or a piezoelectrically actuated material. The other is of the fluid pulsation type, for which the sound wave is generated elsewhere and then transmitted through a conduit with an opening located on the airfoil surface. No matter which type is adopted, mathematically, sound wave so generated can be conceived as resulting from a transpired fluctuating volume flux whose strength either is known (fluid pulsation type) or can be derived equivalently from the membrane motion (structural vibration type). In other words, the sound source pertaining to the present problem is of the "monopole" type as classified in the context of acoustics.

Generally speaking, the physical boundary condition specified on a solid or a transpired surface usually does not involve explicitly the static pressure. Surface static pressure required by the finite volume method ought to be derived using momentum equations subject to the given nonpermeable or specified normal flux conditions:

$$\boldsymbol{u} \cdot \boldsymbol{n} = \begin{cases} 0 & \text{for solid wall} \\ v_w & \text{for wall with blowing or suction} \end{cases} \tag{18}$$

in which v_w is the imposed surface normal velocity that characterizes the sound strength. The density of the issued volume flux can be extrapolated from the adjacent interior cell-averaged values. The determination of the surface pressure, however, must invoke the momentum equations that, as expressed in the computational domain (ξ, η, τ) and combined together with the continuity equation and the metric identity, take the forms[16]

$$\sqrt{\eta_x^2 + \eta_y^2}\frac{\partial p}{\partial n} = -\rho\left\{\bar{U}\left(\eta_x\frac{\partial u}{\partial \xi} + \eta_y\frac{\partial v}{\partial \xi}\right) + \Pi_w\right\} \tag{19a}$$

$$\Pi_w = \begin{cases} 0, & \text{for solid wall} \\ \dfrac{\partial}{\partial \tau}\bar{V}_w + \bar{V}_w\left(\dfrac{\partial u}{\partial \eta}\eta_x + \dfrac{\partial v}{\partial \eta}\eta_y\right), & \text{for wall with blowing or suction} \end{cases} \tag{19b}$$

in which $\bar{U}$ is the ξ-contravariant velocity and $\bar{V}_w (= v_w\sqrt{\eta_x^2 + \eta_y^2} = \dot{m}_w/\rho)$ is the η-contravariant velocity of which the surface mass flux $\dot{m}_w$ is given over the transpired region. The Cartesian velocity components u and v on the wall, however, are obtainable using the zero-flux (solid wall) or the specified normal velocity transpiration v_w and the extrapolated surface tangential velocity. A speculation of Eqs. (19a) and (19b) allows one to find that the contributions to the normal pressure gradient are attributed to two effects implied in terms on the right-hand side: the streamwise flow gradient appearing as a group of terms involving $\partial u/\partial \xi$ and $\partial v/\partial \xi$ and the sound emission effect Π_w due to the surface flux transpiration and the induced velocity gradients $\partial u/\partial \eta$ and $\partial v/\partial \eta$ in the η direction. With all of the terms in Eqs. (19a) and (19b) being properly

treated and differenced, the normal surface pressure gradient $\partial p/\partial n$ can be calculated readily, and the wall pressure can thus be extrapolated using this gradient value and the adjacent cell-averaged quantity.

The formulation described in Eqs. (19a) and (19b) is valid for a distributed-type monopole that spans a finite number of cells with source strengths assigned at the surface boundaries. As a sound source is taken acoustically compact, which is the case where most of the analytic solutions are available, the detailed arrangement of the cell source strengths over the source region is not critical, and only the integrated quantities are significant. In this situation, the present numerical method may encounter spurious oscillations originating from the spike-like distribution of the source strength when one mesh was used to model the sound source. Therefore, a number of source cells are generally required to result in a smooth distribution of the cell source strengths. In the modeling of an acoustically compact source, the requirements that need to be satisfied are that the sum of the weightings of the source strengths must equal to unity and that the weightings should be arranged in such a manner that spherical symmetry of the wave pattern be retained in a still mean flow acoustic simulation. The present study adopts a strategy using three source cells (the number required can be increased) with weightings $\frac{1}{6}$, $\frac{4}{6}$, and $\frac{1}{6}$ for the strength distribution in simulating an acoustic field induced by a (theoretical) point singularity. The simulated results, as will be shown, are found to be in good agreement with the analytic solutions.

In the far field, the outgoing acoustic wave asymptotically approaches a planar one-dimensional wave that enables the use of the nonreflecting boundary conditions based upon the Riemann invariants in the direction normal to the outer boundary.[15] The tangential velocity component and the entropy can be determined using either the freestream values or those extrapolated from the interior, depending upon the direction of propagation of the corresponding characteristic waves.

III. Code Validation

First, to examine the capability of the numerical techniques currently employed, three acoustic wave tests were conducted. All of these test problems have analytic solutions so that the numerical techniques can be evaluated properly.

Two-Dimensional Linear Wave Convection

Most of the upwind schemes currently in use are, strictly speaking, developed based on the one-dimensional framework. The accuracy of the scheme would deteriorate when applied to the multidimensional problems, in particular when the mesh system used is nonuniform and/or highly stretched. To assess the present scheme in this respect, we consider the two-dimensional linear wave convection problem:

$$\frac{\partial u}{\partial t} + \frac{\partial u}{\partial x} + \frac{\partial u}{\partial y} = 0, \text{ in } (0, T) \times \Omega \tag{20}$$

$$u(x, y, t = 0) = \bar{u} + u' \sin[2\pi(x + y)], \qquad (x, y) \in \Omega \tag{21}$$

where the mean value $\bar{u} = 1.0$ and the perturbation amplitude $u' = 0.005$. The domain of interest Ω is confined within a square $-1 \leq x \leq 1$ and $-1 \leq y \leq 1$.

The computational domain was purposely selected to span a period of 2π in both x and y directions so that the periodic boundary condition can be enforced to preclude the involvement of boundary condition accuracy in the present simulation. Physically, this can be taken as observing a linear wave from a convective frame. Hence, the dissipation and dispersion characteristics of the scheme can be evaluated temporally at the instant of interest, $t = T$. The special selection, i.e., $u' \ll \bar{u}$, allows one to access the ability of the present numerical scheme in resolving small disturbances. Note that the convective wave fronts are skewed with respect to the cell faces, hence making the present model problem a good test for the numerical schemes.

In the following cases tested, the uniform Cartesian, nonuniform rectangular (mesh A), and nonuniform and skewed (mesh B) grids were used. Figure 1 depicts the nonuniform mesh systems A and B where mesh B was generated by skewing the cells located at the central portion of mesh A. The largest cell aspect ratio in mesh A is around 4. Figure 2 shows the velocity contour plots computed using the currently developed numerical methods. It can be seen that in general good resolution in the numerical solution was achieved on the uniform Cartesian mesh system. However, as the meshes were stretched or skewed, the consideration of mesh spacings in the construction of interpolated variables at the cell interface, as expressed

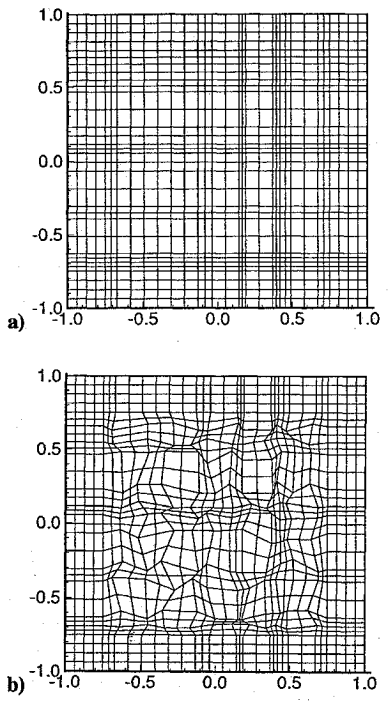

Fig. 1 Nonuniform mesh systems A and B (32 × 32 cells) used for the two-dimensional linear wave convection simulations.

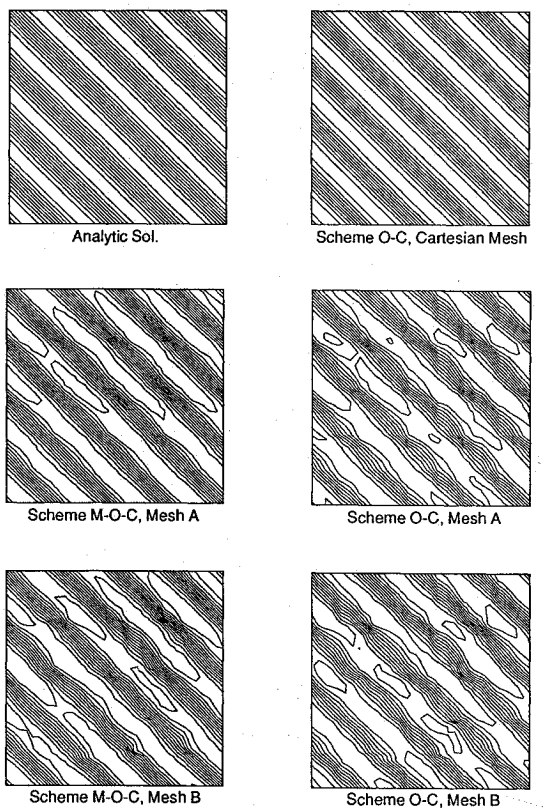

Fig. 2 Velocity contour plots for two-dimensional linear wave convection simulations $\phi = \frac{1}{3}$. Scheme O-C: original Osher-Chakravarthy scheme, Eq. (11), and scheme M-O-C: modified Osher-Chakravarthy scheme, Eq. (9).

Table 1 L_2 and L_∞ errors for two-dimensional linear waves convection simulation ($\phi = \frac{1}{3}$)

Cell number	Scheme[a]	Mesh	L_2 norm		L_∞ norm	
			Error $\times 10^3$	Order	Error $\times 10^3$	Order
16 × 16	O-C	Cartesian	2.916	——	4.187	——
	M-O-C	A	2.999	——	4.507	——
	M-O-C	B	3.044	——	4.630	——
	O-C	A	3.244	——	4.797	——
	O-C	B	3.224	——	4.766	——
32 × 32	O-C	Cartesian	0.651	2.16	1.176	1.83
	M-O-C	A	1.064	1.50	2.118	1.09
	M-O-C	B	1.177	1.37	2.382	0.96
	O-C	A	1.455	1.16	2.718	0.82
	O-C	B	1.454	1.15	2.671	0.84
64 × 64	O-C	Cartesian	0.121	2.42	0.316	1.89
	M-O-C	A	0.245	2.12	0.703	1.59
	M-O-C	B	0.296	1.99	0.916	1.38
	O-C	A	0.386	1.92	1.019	1.42
	O-C	B	0.394	1.88	1.003	1.41

[a]Scheme O-C: original Osher-Chakravarthy scheme, Eq. (11); scheme M-O-C: modified Osher-Chakravarthy scheme, Eq. (9).

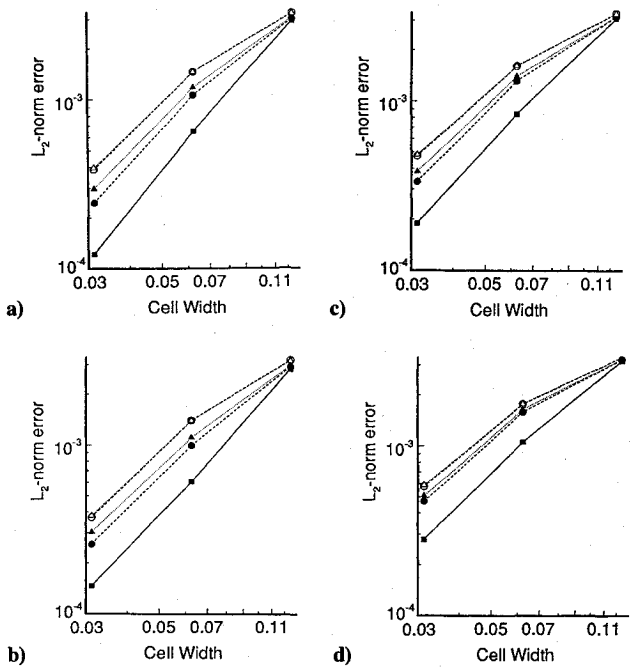

Fig. 3 L_2-norm error vs cell width for two-dimensional linear wave convection simulations; ■: data obtained on uniform Cartesian mesh; •, ○: data obtained on mesh A using scheme M-O-C (•) and scheme O-C (○); and ▲,△: data obtained on mesh B using scheme M-O-C (▲) and scheme O-C (△); a) $\phi = \frac{1}{3}$, b) $\phi = \frac{1}{2}$, c) $\phi = 0$, and d) $\phi = -\frac{1}{3}$.

in Eq. (14), became meaningful for the scheme to yield better resolution for the numerical acoustic simulation. Table 1 displays the detailed comparisons, and from the L_2 and L_∞ error norms it is seen that the modified scheme is superior for simulations performed on the nonuniform meshes.

The scheme accuracy can be quantified on plots using the L_2 norm, as shown in Fig. 3. Four kinds of schemes were selected, i.e., $\phi = \frac{1}{3}, \frac{1}{2}, 0$, and $-\frac{1}{3}$. Generally speaking, for all of the ϕ values examined, the orders of scheme accuracy considering mesh nonuniformity in the reconstruction are relatively higher. But this advantage becomes less prominent when the grid conditions, i.e., the uniformity and skewness, deteriorate. This can be understood since the present correction of interpolation was made on the one-dimensional basis. Any effects that strengthen the multidimensionality of the problem nature may reduce the significance of the present way of scheme improvement. Among these cases examined, the schemes using $\phi = \frac{1}{3}$ and $\frac{1}{2}$ yielded solutions of comparable accuracy. However, the scheme with parameter $\phi = \frac{1}{3}$ will be used in the following acoustic simulations since, theoretically, it can give a third-order accuracy for a scalar one-dimensional simulation on a uniform mesh system.

Baffled Piston Radiation

In this problem and the next one, we test the appropriateness of the numerical boundary condition treatments, including those of the solid boundary, sound source modeling, and the nonreflective far-field boundary. Baffled piston radiation is a standard acoustic model problem that illustrates the directivity of wave propagation. The piston consists of a fluctuating flat plate with width $2d$ and is flush mounted in a hard wall of infinite extent. The vibration of the piston will generate an equivalent volume flow rate, $Q = Q_0 \sin kt$, in and out from the mean piston surface. The surrounding mean flow was at rest, and the acoustic strength was selected to be $Q_0 = \bar{Q}_0/a_\infty d = 5.0 \times 10^{-4}$ and the frequency $k = \omega d/a_\infty = 4.23$, where ω is the circular frequency, and a_∞ is the speed of sound. The analytic solution for the pressure perturbation is available,[17]

$$p'(x, y, t) = \frac{kQ_0}{4}\left\{ \sin kt \int_{-1}^{1} N_0\left[\frac{k}{\sqrt{\gamma}}\sqrt{(x-\eta)^2 + y^2}\right] d\eta + \cos kt \int_{-1}^{1} J_0\left[\frac{k}{\sqrt{\gamma}}\sqrt{(x-\eta)^2 + y^2}\right] d\eta \right\} \tag{22}$$

where γ is the specific heat ratio, and N_0 and J_0 are the Neumann and Bessel functions, respectively.

The computational domain covers a finite region of $-4 \le x \le 4$ and $0 \le y \le 4.5$, and on the bottom boundary the piston spans a segment of $-1 \le x \le 1$. There were around six wavelets contained in the computational domain. Totally there were 280 × 150 Cartesian cells used with 70 cells being located over the piston surface area. The computational time was sufficiently long so that any wave reflection from the outer boundary can influence the simulated data. In general, satisfactory numerical results are found in comparison with the analytic solutions, as shown in the contour plots illustrated in Fig. 4. In Fig. 5, more detailed quantitative comparisons at several vertical positions, $y/d = 0.14, 0.29, 1.40$, and 1.98, are shown. It is observed that in general the acoustic field can be simulated accurately using the present high-resolution algorithm, and even the magnitude of the fluctuation field is very small.

Monopole Radiation in a Compressible Stream

We now consider a uniform stream past a monopole located in a wall of infinite extent. The feature that is new and was not included in the previous baffled piston radiation is the effect of the mean stream

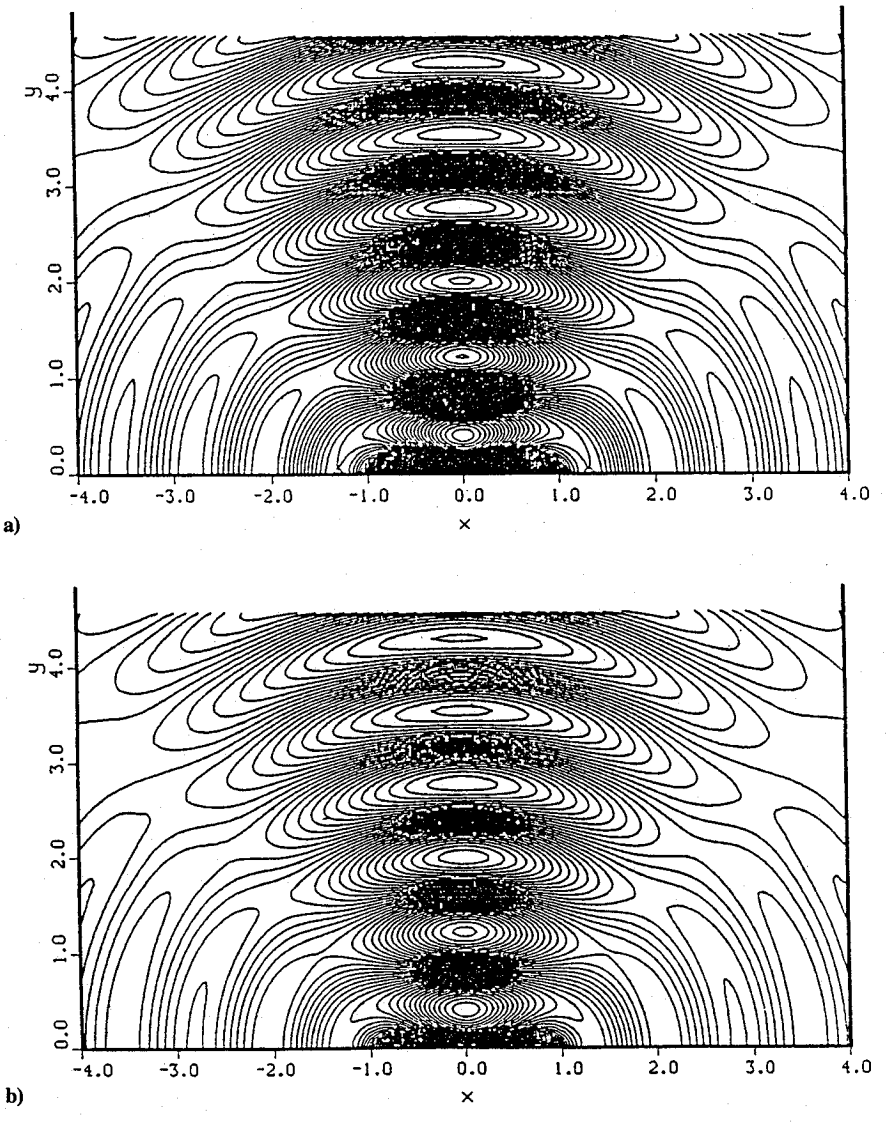

Fig. 4 Pressure contour plots of a baffled piston radiation; $Q = Q_0 \sin kt$, $Q_0 = 5.0 \times 10^{-4}$, $k = 4.23$, and $t = 6.0$; a) analytic solution and b) numerical solution.

convection on the wave propagation. The volume flow rate sent out by the monopole source is $Q = Q_0 \sin 2\pi t$, $Q_0 = 1.0 \times 10^{-4}$ (the nondimensional length and velocity scales are now the still air acoustic wavelength and sound speed, respectively). The analytic pressure perturbation can be expressed as

$$p'(x, y, t) = \mathrm{Re}[\bar{p}(x, y)e^{ikt}] \tag{23a}$$

$$\bar{p}(x, y) = \frac{\pi\gamma Q_0}{M_\infty^2\left(1 - M_\infty^2\right)^{3/2}}\left\{\frac{1}{M_\infty}H_0^{(2)}\left[\frac{2\pi}{1 - M_\infty^2}\times\sqrt{x^2 + y^2\left(1 - M_\infty^2\right)}\right] + i\frac{x}{\sqrt{x^2 + y^2\left(1 - M_\infty^2\right)}}H_1^{(2)}\left[\frac{2\pi}{1 - M_\infty^2}\sqrt{x^2 + y^2\left(1 - M_\infty^2\right)}\right]\right\} \times \exp\left\{i\left[2\pi M_\infty/\left(1 - M_\infty^2\right)\right]x\right\} \tag{23b}$$

where Re denotes the real part of the argument, and $H_0^{(2)}(r)$ and $H_1^{(2)}(r)$ are the Hankel functions constructed using the Bessel functions:

$$H_0^{(2)}(r) = J_0(r) - iN_0(r)$$
$$H_1^{(2)}(r) = J_1(r) - iN_1(r) \tag{24}$$

There are two freestream Mach numbers, $M_\infty = 0.20$ and 0.60, that were selected for the simulations. Figure 6 illustrates the results computed on a stretched mesh system (180 × 90) and the comparisons with the analytic solutions. The inaccuracy found in the upwind direction is due to the lack of grid resolution there, indicating that the grid distribution should be so arranged that the most retarded waves can be resolved properly. This points out a special consideration in defining the spatial grid resolution that might not be obvious for a general acoustic computation, namely, the characteristic length scale of the flowfield may be shrunk by the mean flow convection effect.

IV. Acoustic/Vortical Interaction Simulation

The major concern that differs from the previous ones lies in the generation of an acoustically induced vortical wake downstream of the trailing edge. The present model problem represents a finite plate immersed in parallel to a freestream with a monopole flush mounted on the upper surface of the plate. The exact solution was derived by Lu and Huang,[4] who did analytic work elaborating on the acoustic flutter suppression mechanism. The computational simulation was performed using the currently developed compressible Euler code, in which the freestream Mach number was set to be $M_\infty = 0.1$ to minimize the compressibility effect. The volume flux of the monopole strength was chosen as $Q = Q_0 \sin kt$, $Q_0 = 2.1 \times 10^{-4}$, and $k = \omega c/a_\infty = 0.085$ (now the velocity and length scales are the freestream sound speed a_∞ and the chord length

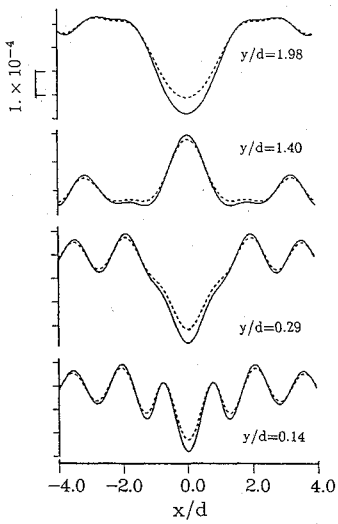

Fig. 5 Pressure fluctuation distributions of a baffled piston radiation, $Q = Q_0 \sin kt$, $Q_0 = 5.0 \times 10^{-4}$, $k = 4.23$, and $t = 6.0$ (solid line: analytic solution, and dash line: numerical solution).

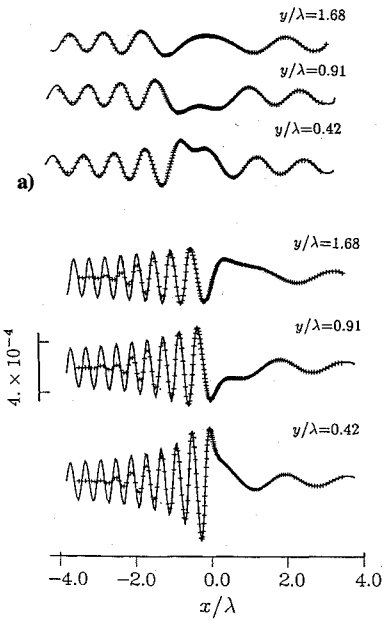

Fig. 6 Pressure fluctuation distributions for monopole radiation in a mean stream above a plane of infinite extent; a) $M_\infty = 0.20$ and b) $M_\infty = 0.60$ (solid line: analytic solution, and +: numerical solution).

of the plate c, respectively). Figure 7 displays an instantaneous pressure fluctuation distribution at some selected instant. In the vicinity of the monopole source, the numerical results show that the velocity acceleration and deceleration induced by the pulsation of the monopole were properly simulated to result in a fore-and-aft asymmetric distribution of the perturbation pressure field. At the leading edge and the location of the monopole, the theoretical results contain singularities, although the real physical flow and the numerical results are finite there. It is observed that over these singular regions the trend of rapid flowfield variation predicted by the theoretical analysis was well captured by the numerical scheme. The integrated lift and pitching moment coefficients, C_L and C_M, are shown in Fig. 8. Small-scale fluctuations are found with the computed C_L and C_M curves. They are believed to be caused by the local errors convected from the sharp leading edge where the grid resolution was not sufficient. Airfoils with finite radius noses were also simulated,[16] and the computed solutions, however, appeared to be smooth.

An important physical feature that is unique to the present problem is the production of the vortical part in the original irrotational

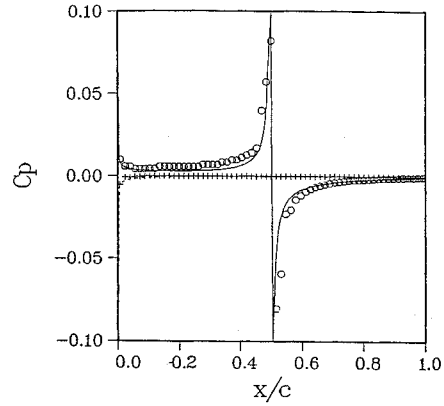

Fig. 7 Pressure distributions induced by a monopole sound source on a finite flat plate, $Q = Q_0 \sin kt$, $Q_0 = 2.1 \times 10^{-4}$, and $k = 0.085$ (solid line: analytic solution, upper surface; dash line: analytic solution, lower surface; o: numerical solution, upper surface; and +: numerical solution, lower surface).

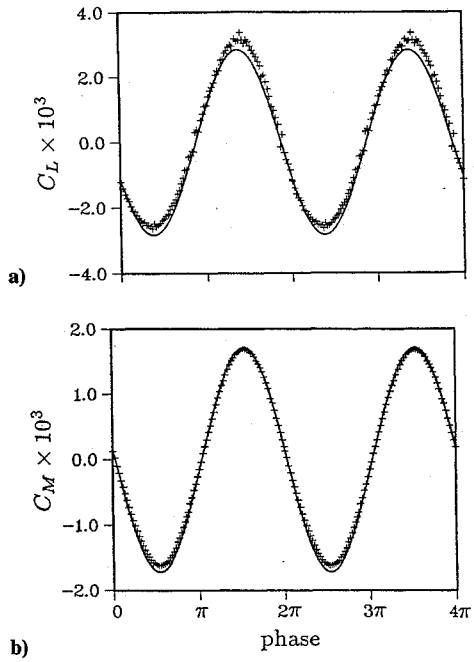

Fig. 8 Unsteady airloads induced by a monopole sound source on a finite flat plate, $Q = Q_0 \sin kt$, $Q_0 = 2.1 \times 10^{-4}$, and $k = 0.085$; a) lift coefficient and b) pitching moment coefficient (solid line: analytic solution, and +: numerical solution).

flow. As was explained by Lu and Huang,[4] the acoustically induced shedding vortices result from the satisfication of Kutta condition at the trailing edge. The definition of the shedding vortex strength in a potential flow analysis can be given by the tangential velocity jump across the wake cut:

$$\gamma_w = \int_\delta (\nabla \times \boldsymbol{u})\, dy \approx \int_\delta \left(-\frac{\partial u}{\partial y} \right) dy = u_l - u_u \qquad (25)$$

in which δ is the shear layer thickness, and u_u and u_l denote the tangential velocities above and beneath the wake cut, respectively.

The present numerical treatment of the Euler equations did not explicitly enforce the artificial Kutta condition[18] as did the potential flow analysis. However, it is shown in Fig. 9 that the computed wake profiles agree well with the theoretical predictions except for the distributions around the trailing edge and in the far downstream. As explained by Rizzi,[18] it is the numerical dissipation that mimics the physical viscous effect over the trailing-edge region that enables the present inviscid Euler flow solver to give a good description of the wave/vorticity interaction around the sharp trailing edge. Figure 10 shows the tangential velocity

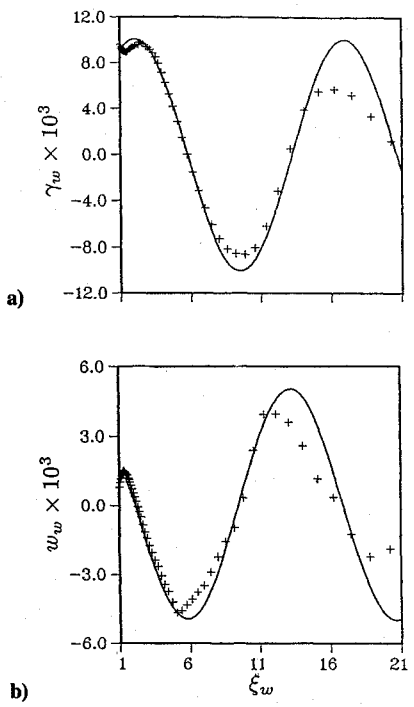

Fig. 9 Wake flow characteristics produced by a monopole sound source on a finite flat plate, $Q = Q_0 \sin kt$, $Q_0 = 2.1 \times 10^{-4}$, $k = 0.085$, and phase angle = $2\pi/6$; a) vortex strength distribution and b) downwash distribution (solid line: analytic solution, and +: numerical solution).

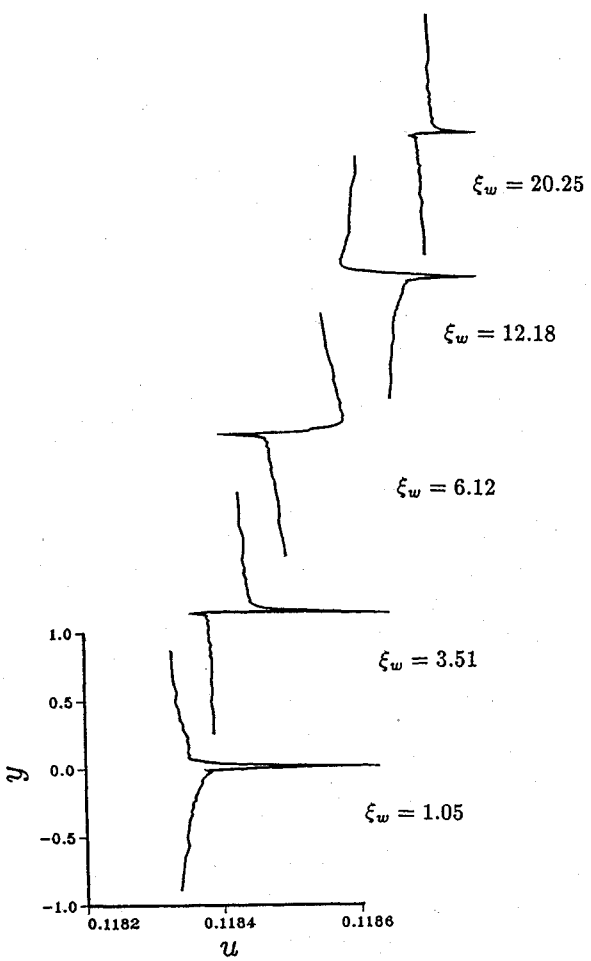

Fig. 10 Tangential velocity distributions across the wake produced by a monopole sound source on a finite flat plate, $Q = Q_0 \sin kt$, $Q_0 = 2.1 \times 10^{-4}$, and $k = 0.085$.

distributions on five representative sectional planes perpendicular to the wake cut. Since the numerical dissipation plays the role of physical viscosity, therefore, a finite thickness wake shows up in the present simulation. Unusual spike-like velocity distributions are found around the wake center. This phenomenon is not physical, and the cause for this anomaly could possibly be due to the Riemann solver employed in the flux-difference scheme, since, theoretically, the one-dimensional Riemann solver based on the dimension-split method cannot cope with the discontinuities aligned orthogonally to the flow direction. Therefore, a judicious judgment is necessitated in defining the wake edge velocities u_u and u_l. The computed γ_w results plotted in Fig. 9 were obtained using Eq. (25) while keeping in mind that the spurious spike-like jumps should be ignored.

Trailing-edge flow possesses a very complicated flow structure[9,10] that undergoes an abrupt transition from wall boundary layer to free shear layer. The potential flow analysis cannot give a full description of this strong viscous/inviscid interaction problem, nor can the present inviscid scheme that relies essentially on the nonphysical numerical dissipation. The reason causing solution discrepancy around the trailing edge, at the present time, is not clearly known. Further investigation is necessary that calls for the use of a high-resolution Navier–Stokes solver in the future. The inconsistency appearing in the far downstream results, however, comes from the lack of grid resolution there. Accuracy can be improved when more grids are used in the downstream.

It is worth mentioning that the present acoustically induced vortical flow is in principle a phenomenon resulting from the satisfaction of Kutta condition at the trailing edge. Therefore, for the present problem, the inviscid Euler flow model is considered sufficient since the results show that Kutta condition is always satisfied at the trailing edge. The induced circulatory flow is seen to be well captured, which can be evidenced from the calculated C_L and C_M data when compared with the analytic solutions.

V. Concluding Remarks

A numerical scheme capable of solving the near-field aeroacoustic problems was developed. The acoustic accuracy was achieved by improving the interpolation of the cell interface variables of the flux-difference scheme. This interpolation, which takes into account the grid nonuniformity property, is in practice a significant procedure for treating wave propagation problems on a stretched mesh system. The numerical boundary treatment of a flush-mounted monopole was also devised. This aeroacoustic flow solver has been validated by checking with acoustic model problems having analytic solutions.

Wave/vortex interaction around a sharp trailing edge was simulated using the currently developed scheme. The results agree well with the analytic solutions. Although the Kutta condition was not explicitly enforced, the numerical dissipation enabled the present Euler flow solver to correctly predict the induced unsteady airloads. Inadequacy of the scheme was found in the wake flow simulation, where tangential discontinuities were hard to be correctly captured by the one-dimensional Riemann solver and the dimension-split method employed in the present flux-difference scheme.

In summary, it is concluded that the currently developed high-resolution upwind scheme can be used for predicting small flow perturbations provided that sufficient grid resolution was used. Acoustically induced vortices and airloads have been satisfactorily predicted numerically in a quite general manner. This provides confidence in the future application of the present scheme to problems involving more complex and/or nonlinear interactions of the waves.

References

[1]Huang, X.-Y., "Active Control of Airfoil Flutter," *AIAA Journal*, Vol. 25, No. 8, 1987, pp. 1126–1132.

[2]Thomas, J. P., and Roe, P. L., "Development of Non-Dissipative Numerical Schemes for Computational Aeroacoustics," AIAA Paper 93-3382-CP, July 1993.

[3]Tam, C. K. W., and Webb, J. C., "Dispersion-Relation-Preserving Finite Difference Schemes for Computational Aeroacoustics," *Journal of Computational Physics*, Vol. 107, No. 2, 1993, pp. 262–281.

[4]Lu, P.-J., and Huang, L.-J., "Flutter Suppression of Thin Airfoils Using Active Acoustic Excitations," *AIAA Journal*, Vol. 30, No. 12, 1992, pp. 2873–2881.

[5]Crighton, D. G., "Acoustic as a Branch of Fluid Mechanics," *Journal of Fluid Mechanics*, Vol. 106, May 1981, pp. 261–298.

[6]Lighthill, M. J., "Acoustic Streaming," *Journal of Sound and Vibration*, Vol. 61, No. 3, 1978, pp. 391–418.

[7]Wu, J.-Z., and Wu, J.-M., "A Theoretical Formulation of Wave Vortex Interactions," AIAA Paper 89-0988, March 1989.

[8]Wu, J.-Z., Vakili, A. D., and Wu, J.-M., "Review of the Physics of Enhancing Vortex Lift by Unsteady Excitation," *Progress in Aerospace Sciences*, Vol. 28, No. 2, 1991, pp. 73–131.

[9]Daniels, P. G., "On the Unsteady Kutta Condition," *Quarterly Journal of Mechanics and Applied Mathematics*, Vol. 31, Pt. 1, 1978, pp. 49–75.

[10]Crighton, D. G., "The Kutta Condition in Unsteady Flow," *Annual Review of Fluid Mechanics*, Vol. 17, 1985, pp. 411–445.

[11]Roe, P. L., "Approximate Riemann Solvers, Parameter Vectors, and Difference Schemes," *Journal of Computational Physics*, Vol. 43, No. 2, 1981, pp. 357–372.

[12]Chakravarthy, S. R., and Osher, S., "A New Class of High Accuracy TVD Schemes for Hyperbolic Conservation Laws," AIAA Paper 85-0363, Jan. 1985.

[13]van Leer, B. "Towards the Ultimate Conservative Difference Scheme. II. Monotonicity and Conservation Combined in a Second-Order Scheme," *Journal of Computational Physics*, Vol. 14, No. 2, 1974, pp. 361–370.

[14]Liou, M.-S., and Hsu, A. T., "A Time Accurate Finite Volume High Resolution Scheme for Three Dimensional Navier–Stokes Equations," AIAA Paper 89-1994, June 1989.

[15]Venkatakrishnan, V., and Jameson, A., "Computation of Unsteady Transonic Flows by the Solution of Euler Equations," *AIAA Journal*, Vol. 26, No. 8, 1988, pp. 974–981.

[16]Yeh, D.-Y., "Unsteady Aerodynamic and Aeroelastic Behaviors of Acoustically Excited Transonic Flow," Ph. D. Dissertation, Inst. of Aeronautics and Astronautics, National Cheng Kung Univ., Tainan, Taiwan, ROC, 1992.

[17]Dowling, A. P., and Ffowcs Williams, J. E., *Sound and Sources of Sound*, Wiley, New York, 1983.

[18]Rizzi, A., "Damped Euler Equation Method to Compute Transonic Flow Around Wing-Body Combinations," *AIAA Journal*, Vol. 20, No. 10, 1982, pp. 1321–1328.